Reversible Iron Exsolution

DOI: 10.1002/ange.201404476

# Reversible Topochemical Exsolution of Iron in $BaFe^{2+}_2(PO_4)_2$**

*Rénald David, Houria Kabbour, Dmitry Filimonov, Marielle Huvé, Alain Pautrat, and Olivier Mentré**

***Abstract:*** *$BaFe^{2+}_2(PO_4)_2$ was recently prepared and identified as the first 2D-Ising ferromagnetic oxide with an original reentrant structural transition driven by high-spin $Fe^{2+}$ ions arranged in honeycomb layers. Both long-term air exposure and moderate temperature ($T > 375\,°C$) leads to topochemical oxidation into iron-depleted compounds with mixed $Fe^{2+}/Fe^{3+}$ valence. This process is unique, as the exsolution is effective even from single crystal with preservation of the initial crystallinity, and the structure of the deficient $BaFe_{2-x}(PO_4)_2$ ($x <$ ca. 0.5) is fully ordered for $x = 2/7$ and 1/3 with creation of novel original depleted triangular lattices. Under flowing $H_2$/Ar, Fe is reincorporated in the structure above 480 °C, as reproduced under the electron beam in a transmission microscope. After Fe exsolution, the insulating ferromagnetic compound turns into an antiferromagnetic semiconductor.*

Topochemical modifications of solid oxides enable the tuning of structural and physical properties in a remarkable manner but most often involve changes of the anionic sublattice balanced by metal redox centers.[1] Recent spectacular examples concern the reduction by hydrides, leading to dramatic oxygen sub-stoichiometry (for example, $SrFeO_2$ with square planar $Fe^{2+}O_4$ units[2]) or the unexpected $H^-$ incorporation in oxyhydrides (for example, $BaTiO_{3-x}H_x$[3]). Besides, the topochemical modification of the cationic sublattice mainly concerns the intercalation/desintercalation of mobile ions, that is, alkali ions. Most rarely, the metal framework itself participates in an exsolution phenomenon. Representative examples include $nCuO\text{-}V_2O_5$ and $Cu_{2.33}V_4O_{11}$ oxides,[4,5] with reversible exsolution of $Cu^0$ into dendrites in the latter, during Li intercalation.[6] Also, a handful of compounds exhibit a spontaneous exsolution of cations at moderate temperature, for example, the olivine $LiFePO_4$ and $Fe_2SiO_4$.[7–9] This rare behavior seems favored for ferrous $Fe^{2+}$ ions, reminiscent of the exsolution of Fe-rich inclusions out of minerals or meteorite rocks.[10,11] Our search for new candidates for such reactions focuses on the recent $BaFe^{2+}_2(PO_4)_2$ compound.[12] Its layered crystal structure ($a =$ 4.8730(2) Å, $c = 23.368(2)$ Å, space group $R\bar{3}$) is shown in Figure 1a. This compound is a unique case of a true 2D-ferromagnetic Ising oxide with $Fe^{2+}$ spins ($S = 2$) below $T_c =$ 65.5 K.[12] Furthermore, it displays a fascinating re-entrant structural transition following the sequence : $R\bar{3}$ (RT, paramagnetic)→ $P\bar{1}$ (140 K, paramagnetic)→ $R\bar{3}$ (ca. 70 K, ferromagnetic) that is driven by the competition between the lattice Jahn–Teller instability and the energy gained through the uniaxial ferromagnetic ordering.[13,14] This atypical behavior questions about the high temperature stability. Indeed, $BaFe_2(PO_4)_2$ has all requirements for enhanced

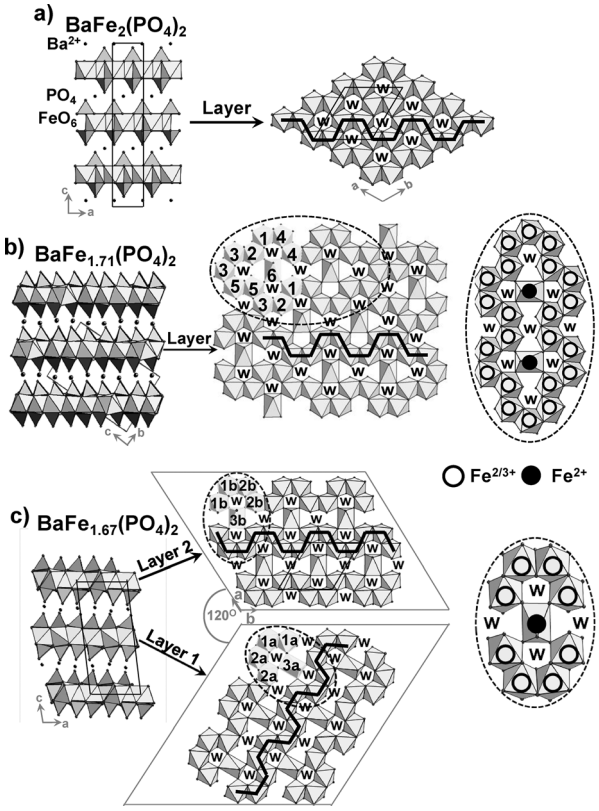


***Figure 1.*** a) Layered crystal structure of the pristine $BaFe_2(PO_4)_2$ compound. W denotes the honeycomb windows. b), c) Crystal structure and charge distribution for b) $BaFe_{1.71}(PO_4)_2$ and c) $BaFe_{1.67}(PO_4)_2$ with evidence of the two independent depleted layers 120° tilted. The continuous line shows unmodified octahedral chains.

[*] Dr. R. David, Dr. H. Kabbour, Prof. Dr. M. Huvé, Dr. O. Mentré
Univ. Lille Nord de France, CNRS UMR8181
Unité de Catalyse et de Chimie du Solide, UCCS USTL
F-59655 Villeneuve d'Ascq (France)
E-mail: olivier.mentre@ensc-lille.fr
Dr. A. Pautrat
CRISMAT, UMR 6508-CNRS, ENSICAEN, Caen (France)
Dr. D. Filimonov
Department of Chemistry
M. V. Lomonosov Moscow State University, 119991 Moscow (Russia)

[**] This work was carried out under the framework of the MAD-BLAST project supported by the ANR (Grant ANR-09-BLAN-0187-01). The ANR (grant number: ANION-CO,12-JS08-0012) is thanked for financial support as well as the region Nord pas de Calais for funding XRD systems.

Supporting information for this article is available on the WWW under http://dx.doi.org/10.1002/anie.201404476.

  

reactivity with air because: 1) $Fe^{2+}$ ions form bidimensional (2D) honeycomb layers separated by a large interleaf of about 7.8 Å that may favor cationic diffusion; 2) all of the oxygen anions are strongly bonded through covalent P–O bonds stabilizing the anionic sub-lattice; and 3) in contrast to M = $Ni^{2+}$ and $Co^{2+}$, $BaM_2(PO_4)_2$ isomorphs prepared by solid-state reaction in air,[15–17] $BaFe_2(PO_4)_2$ can only be obtained in solvothermal conditions (hydrazine dilute solution).[12] Herein, we present various $BaFe_{2-x}(PO_4)_2$ phases obtained after Fe exsolution. This phenomenon is reversible, thermally activated but also efficient at room temperature, and leads to novel fully ordered Fe-depleted 2D triangular lattices for $x = 2/7$ and $x = 1/3$.

First evidence for moderate Fe exsolution were found after aging large $BaFe_2(PO_4)_2$ single crystals held on a glass plate in polymonotrifluorochloroethylene (PTFCE) grease after about 12 months in air at room temperature. Yellow crystals turn black with formation of reddish surfacial islets (Figure 2). The EDX mapping shows a homogeneous distribution of Ba, Fe, and P in the bulk while rust-like dots are composed of iron oxide. Strikingly, the iron exsolution is not destructive, because large crystalline single domains were extracted from the resulting blocks. The corresponding crystal structure was refined in a triclinic unit cell leading to a fully ordered $BaFe_{12/7}(PO_4)_2$ stoichiometry ($P\bar{1}$ space group, $a = 8.3380(5)$ Å, $b = 9.8508(6$ Å, $c = 14.4567(8$ Å, $\alpha = 90.722(3)°$, $\beta = 94.579(3)°$, $\gamma = 106.812(3)°$, $R = 4.76\,\%$, $wR = 5.26\,\%$, see details in the Supporting Information, Section S2). The crystal structure remains 2D though a modification of the initial honeycomb layers, as shown in Figure 1b. The arrangement between the Kagomé windows with apical $PO_4$ groups is fully preserved but distorted, while Fe ions are rearranged owing to the exsolution of 1/7th of them. In the $_\infty\{Fe_{12/7}O_6\}$ octahedral sheets, 5/7th of the $FeO_6$ remain regular (Fe1–Fe5 labels), 1/7th are strongly distorted (Fe6 label) and 1/7th are vacant. The refined formula indicates a mean $Fe^{2.33+}$ valence state, compatible with our bond valence sum (BVS) calculation:[18] it leads to a mixed $Fe^{2+}/Fe^{3+}$ distribution on Fe1–Fe5 sites, and $Fe^{2+}$ ions on Fe6 positions. At this stage, PTFCE being chemically inert, the room-temperature topochemical Fe exsolution suggests an easy thermal activation concomitant with the oxidation of the host lattice. Owing to the long maturation process, it was not possible do date to obtain a homogeneous sample for further characterization.

The activation of this phenomenon in a more controlled manner was processed by heating polycrystalline $BaFe_2(PO_4)_2$ material in air. The thermogravimetric analysis (TGA) plot shows a progressive weight gain starting above about 250 °C, indicating a continuous oxidation (Figure 3a). From both TGA and in situ thermal X-ray diffraction (XRD) analysis (Supporting Information, Section S1), it could be sequenced in successive steps. First, between 375 °C and 600 °C, progressive Fe exsolution occurs, leading to $Fe_2O_3$ and novel $BaFe_{2-x}(PO_4)_2$ triclinic phases that are different from the $x = 2/7$ phase. Between 550 °C and 650 °C the pristine compound is fully transformed. The exsolution is assigned to the following reaction:

$$BaFe^{2+}{}_2(PO_4)_2 + 3x/4\,O_2 \rightarrow BaFe^{2/3+}{}_{2-x}(PO_4)_2 + x/2\,Fe^{3+}{}_2O_3$$

From TGA, we find $x$ is less than about 0.54, which corresponds to a 3 wt% loss. The absence of peaks at particular $x$ values indicates a continuous process, see Figure 3a. Second, Above 650 °C, the Fe-deficient compound transforms into the cubic $Ba_{1.5}Fe^{3+}{}_2(PO_4)_3$ Langbeinite type,[19] while the weight gain stops around 700 °C.

Figure 3b shows the evolution of the lattice parameters refined from HT-XRD patterns plotted in the triclinic base, according to the rhombohedral/triclinic relation given below. In the initial rhombohedral domain (RT to 375 °C), focusing on the most temperature dependent c parameter, we find

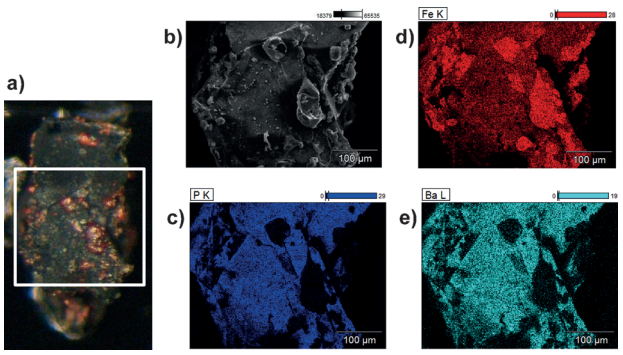


***Figure 2.*** Fe-exsoluted crystal after 12 months aging in PTFCE grease in air. a) optical micrograph, b) MEB image; c) phosphorus d) iron, and e) barium mapping from EDX analysis.

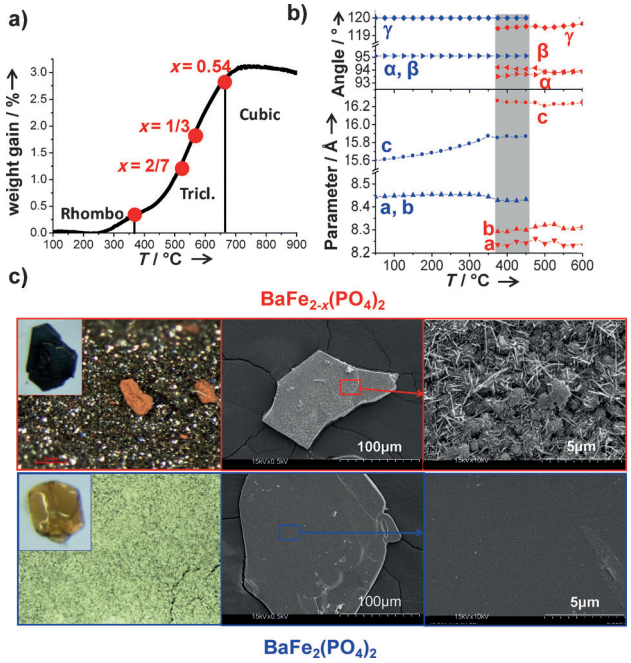


***Figure 3.*** a) TGA curve of $BaFe_2(PO_4)_2$ with evidence of the major phase determined from HT-XRD. b) Lattice parameters against temperature in the triclinic orientation. c) From $BaFe_2(PO_4)_2$ powder and crystals to the depleted form. The $Fe_2O_3$ clusters are seen at the crystal edges.

a thermal expansion coefficient (TEC $= \Delta c/c_0 \cdot \Delta T$) of $59 \times 10^{-6}\,°C^{-1}$. In the triclinic region ($350 < T < 600\,°C$), the TEC is negligible, while the system keeps oxidizing. It suggests a monotonic Fe exsolution, while the volume contraction owing to creation of vacancies is balanced by the thermal lattice expansion.

The color change from yellow-greenish (pristine) to black (Fe-depleted compound) is shown in Figure 3c before and after heating polycrystalline and single-crystal samples at 550 °C for 5 h. Some reddish grains can also be observed which correspond to the coating of some grains by $Fe_2O_3$. The SEM images of heated crystal show a damaged surface after exsolution owing to $Fe_2O_3$ nanometric wires popping out of the faces (see Figure 3c). Once more, large single domains suitable for single crystal XRD analysis were extracted from the heated crystalline blocks, leading to the full-structure resolution.

Details of the crystal structure refinement are given in the Supporting Information, Section S3. It was solved and refined in the triclinic cell: $a = 8.3198(8)$ Å, $b = 8.3276(12)$ Å, $c = 16.306(2)$ Å, $\alpha = 94.65(1)°$, $\beta = 94.995(8)°$, $\gamma = 119.853(6)°$ with $R = 7.07\,\%$, $wR = 7.51\,\%$. The relation between the rhombohedral and triclinic cells is given by: $a_T = -a_R + b_R$, $b_T = -a_R - 2b_R$, $c_T = 2/3\,a_R + 1/3\,b_R - 2/3\,c_R$. The full indexation of diffracted spots involves three twinned domains related by about 120° around $c^*$ (refined ratio: ca. 61 %: ca. 22 %: ca. 17 %). The fully ordered refined structure corresponds to the $BaFe_{1.67}(PO_4)_2$ formula, that is, $x = 1/3$, with 4/6th of regular octahedra ($Fe1_{a,b}$ $Fe2_{a,b}$), 1/6th of strongly distorted sites ($Fe3_{a,b}$), and 1/6th of extra vacancies (Figure 1c). The gradual Fe depletion between discrete $x = 0$, $x = 2/7$, and $x = 1/3$ states is performed through the conservation in the three structures of unchanged zigzag $FeO_6$ chains evidenced by solid lines in Figure 1a–c. For $x = 1/3$, two crystallographic independent $_\infty\{Fe_{5/3}O_8\}$ layers coexist at $z = 0$ and $z = 1/2$ (prefixes a and b were given to the corresponding positions), tilted by about 120° from each other. From the viewpoint of crystallography, it is noteworthy that the complementary 240° tilted motif does not exist, out of twinning domains. The calculated Fe valence is +2.41. Similarly to the $x = 2/7$ case, BVS calculations[18] suggest a mixed $Fe^{2+}/Fe^{3+}$ distribution on regular sites ($Fe1_{a,b}$ $Fe2_{a,b}$), while $Fe^{2+}$ ions occupy the distorted positions ($Fe3_{a,b}$). According to this model, the mean $Fe^{2.5+}$ valence on regular octahedra leads to the iron valence $Fe^{2.41+}$ inferred from crystallography.

The iron valence state was analyzed by Mössbauer spectroscopy on a polycrystalline sample prepared by heating $BaFe_2(PO_4)_2$ at 550 °C for 5 h (Supporting Information, Section S4). The same sample was used for further transport and magnetic characterizations. According to the possible Fe-depletion until $x \approx 0.54$ deduced by TGA, the powder composition may differ significantly from those of the fully $x = 1/3$ ordered single crystal. However, the latter crystallographic model was taken as a reference for our assignment of the spectral contributions. Mössbauer spectra, measured over the temperature range 78–523 K, are different from those of $BaFe_2(PO_4)_2$ (Figure 4a).[13] After Fe exsolution, they consist of overlapping paramagnetic doublets together with magnetic sextets of α-$Fe_2O_3$. At 78 K (Figure 4c), it was fitted using

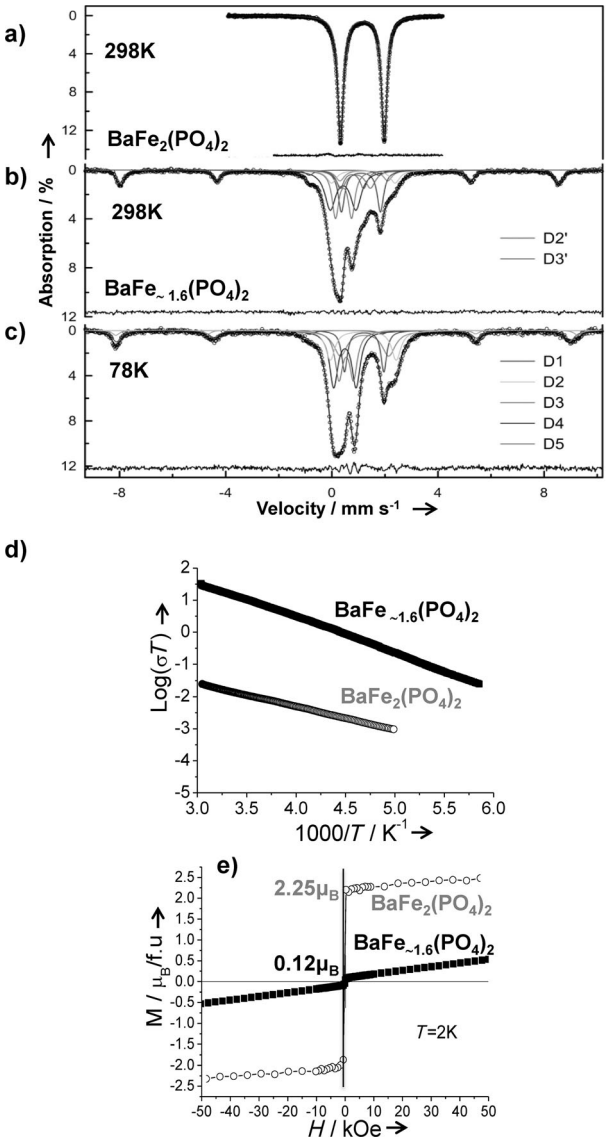


***Figure 4.*** Mössbauer spectra of a) $BaFe_2(PO_4)_2$ at RT and b), c) $BaFe_{1.6}(PO_4)_2$ at b) RT and c) 78 K. d), e) Comparison of the physical properties between the pristine and the depleted compound ($x \approx 0.4$). d) Arrhenius plots of the electric conductivity; e) magnetization at 2 K.

a minimal set of 5 doublets D1–D5 assigned to $Fe^{2+}$ or $Fe^{3+}$ according to their hyperfine parameters and spectral contributions. Two of them correspond to $Fe^{2+}$ in regular $Fe1,2_{a,b}$ octahedral sites (D2 ≈ 15 % and D3 ≈ 21 %) and the two others to $Fe^{3+}$ in the same $Fe1,2_{a,b}$ sites (D4 ≈ 26 % and D5 ≈ 24 %). The latter doublet (D1 ≈ 14 %) is assigned to $Fe^{2+}$ in the strongly distorted Fe3 sites. It represents about 14 % of the total iron content (vs. 20 % calculated from crystallography for the ideal $BaFe_{1.67}(PO_4)_2$) structure. It suggests that for $x > 1/3$ the extra vacancies preferentially concern the distorted sites. It was also confirmed by powder neutron diffraction (PND) data collected on an even more Fe-deficient sample (Supporting Information, Section S5).

All the doublets but D1 are broadened, especially for $Fe^{2+}$, indicating incomplete ordering in the polycrystalline $BaFe_{2-x}(PO_4)_2$ sample or possible inhomogeneities. The

  

refined $Fe^{3+}$:$Fe^{2+}$ ratio is close to 1:1 leading to a mean $BaFe^{2.5+}_{\approx 1.6}(PO_4)_2$ formula close to results from single crystal data, that is, $BaFe^{2.41+}_{1.67}(PO_4)_2$. The formula deduced from Mössbauer was considered for treatment of the physical properties measured on this polycrystalline sample. Note that only a minor part of $Fe_2O_3$ produced by oxidation (ca. 1/5 of the total $Fe_2O_3$ contribution) undergoes an incomplete Morin transition, consistently with a majority of nanometric $Fe_2O_3$ clusters (Figure 3c). As the temperature increases from 78 K to 473 K, the broad D2 and D3 ($Fe^{2+}$) contributions gradually transform into D2′ and D3′ that show significantly lower ISs and $\Delta E_Q$s values (Figure 4b). The D4 and D5 ($Fe^{3+}$) contributions remain nearly unchanged. This result provides a clue for mutual occupancy of the Fe1,2 sites by both $Fe^{2+}$ and $Fe^{3+}$ cations. It is probable that increasing the temperature averages local structures of both voluminous $Fe^{2+}O_6$ and smaller $Fe^{3+}O_6$ octahedra in the same crystallographic sites, leading to smaller $Fe^{2+}O_6$ units with more covalent Fe–O bonds, and accordingly decreasing IS and $\Delta E_Q$ values.[2,21]

The total contributions of the individual $Fe^{2+}$ and $Fe^{3+}$ components were found to be mainly temperature-independent, indicating the absence of electron transfer between $Fe^{2+}$ and $Fe^{3+}$ sites, contrarily to examples such as $Fe_2OBO_3$[20] and $Fe_3O_4$.[21] This result is in accordance with localized states and semiconducting behavior of $BaFe_{\approx 1.6}(PO_4)_2$ discussed below.

The reversibility of the Fe exsolution was verified in situ under reducing atmosphere (flowing 3% $H_2$ in argon) by high-temperature XRD, starting from a $BaFe_{2-x}(PO_4)_2 + x/2\,Fe_2O_3$ biphasic mixture obtained after heating $BaFe_2(PO_4)_2$ (Figure 5a). At 480 °C, the diffraction peaks of $Fe_2O_3$ are significantly weakened while the re-incorporation of Fe is completed at 600 °C. It leads to the single-phase $BaFe_2(PO_4)_2$ recovering its original crystallinity and lattice parameters. Even single crystals with good quality can be recovered from the $H_2$ treatment (Supporting Information, Section S6). The mechanism for such long Fe diffusion into $Fe_2O_3$ clusters is questionable, especially taking into account the room temperature exsolution mentioned above. Insights were given by transmission electron microscopy (TEM). The ED patterns of crushed $BaFe_{5/3}(PO_4)_2$ crystals provide evidence of supercell spots fully indexed in the corresponding triclinic lattice. They vanish after about 15 minutes of electron beam exposure, leading to the subcell $R\bar{3}$ ED pattern (Figure 5b). Concomitantly, a progressive amorphization from the thin edges of crystals towards the thickest core was observed. It suggests that iron ions necessary to fill the vacancies diffuse by contact according to a shrinking core model. The amorphization of the edges can be understood by the difficulty to maintain a periodic framework in exaggeratedly Fe-depleted domains. Details of our TEM analysis are given in the Supporting Information, Figure S7. We checked that similar topochemical metal exsolutions do not occur in isomorphous $BaCo_2(AsO_4)_2$ and $BaNi_2(PO_4)_2$ compounds, even after heating in flowing $O_2$ atmosphere. Then, the diffusion mechanism is presumably driven by the $Fe^{2+}/Fe^{3+}$ redox potential, reminiscent of the oxidation of the olivine $LiFe^{2+}PO_4$ and $Fe^{2+}{}_2SiO_4$ fayalite, leading to $LiFe^{3+}_{1-x}PO_4$ ($x < 1/3$) and $Fe_{2-x}SiO_4$ laihunite types[9] with similar creation of $Fe_2O_3$ nanoclusters.[7,8] A common parameter between all these compounds is

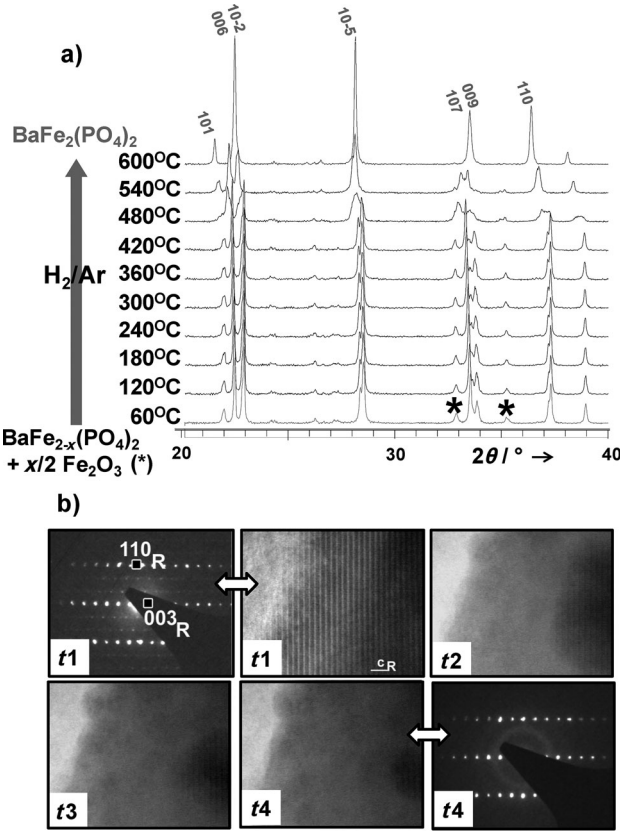


***Figure 5.*** Re-incorporation of Fe in $BaFe_{2-x}(PO_4)_2$ leading back to the rhombohedral form : a) by HT-XRD under flowing $H_2$/Ar, b) in situ in a TEM. Images were taken at $t1 \approx 0$ min, $t2 \approx 5$ min, $t3 \approx 10$ min and $t4 \approx 15$ min.

the presence of $XO_4$ groups connected to a great number of $Fe^{2+}$ ions, for example, 6 in $BaFe_2(PO_4)_2$, therefore able to compensate the creation of cation vacancies by modification of their bonding scheme. However, the reversible exsolution at the single-crystal scale into $BaFe_{2-x}(PO_4)_2$ ordered compounds, even at room temperature, is unique and presumably favored by the 2D topology. Here, by comparison between the layers for $x = 0$, $x = 2/7$, and $x = 1/3$, in-plane diffusion paths could be proposed along corner-sharing octahedral chains. A molecular dynamics study is in progress to obtain a fuller understanding of the mechanism involved. At least, the reversible exsolution of cations could be a source of inspiration for future self-regenerative intelligent catalysts similarly to reversible Pd exsolution from perovskite lattice, but enhanced in layered strucures.[22]

Preliminary synthesis of the pristine $BaFe_2(PO_4)_2$ was originally motivated by the achievement of truly disconnected 2D ferromagnetic compounds with exotic magnetic behaviors,[23] for example, 2D Ising ferromagnetism. Interesting magneto-transport coupling could be expected. However, $BaFe_2(PO_4)_2$ is a single-valent $Fe^{2+}$ insulator, which restricts spin-dependent transport properties that are attractive in the field of low-D materials for data storage.[24–26] The conductivity measurements on platelet crystals (main $\sigma_{ab}$ contribution) evidences a semiconducting behavior for Fe-depleted $BaFe_{\approx 1.6}(PO_4)_2$, leading to an increase of σ by about three

orders of magnitude after Fe-exsolution (Figure 4d). For both compounds, the Arrhenius plots give comparable activation energies $E_a$ of 0.14 eV and 0.19 eV for $BaFe_2(PO_4)_2$ and $BaFe_{\approx 1.6}(PO_4)_2$. Our UV/Vis spectroscopy analysis did not allow us to extract accurate bandgaps (Supporting Information, Section S8). At least the iron exsolution allows significant improvement of the electronic transport.

The magnetic susceptibility of $BaFe^{2.5+}_{ca.1.6}(PO_4)_2$ was fitted by a Curie–Weiss law $\chi = C/(T-\theta_{CW}) + \chi_{hem}$, where $\chi_{hem}$ is the ferromagnetic contribution of the nano-sized superparamagnetic $Fe_2O_3$ hematite,[27] (Supporting Information, Section S9). We found $C = 6.01\ emu\,Oe^{-1}\,mol^{-1}\,K^{-1}$ ($\mu_{eff} = 5.48\ \mu_B/Fe$), $\theta_{CW=} -29.2$ K, and $\chi_{hem} = 3.9.10^{-2}\ emu\,Oe^{-1}\,mol^{-1}$. $\mu_{eff}$ is consistent with the spin-only value of 5.43 $\mu_B$/Fe calculated for $BaFe^{2.5+}_{1.6}(PO_4)_2$. $\chi_{hem}$ matches well the 14% hematite contribution deduced from Mössbauer spectroscopy. Predominant antiferromagnetic $Fe^{3+}$-O-$Fe^{2+}$ and $Fe^{3+}$-O-$Fe^{3+}$ exchanges[28] are revealed by the negative $\theta_{CW}$. Below 80 K, the ZFC/FC divergence shows weak ferromagnetism with a remanent moment of about $0.2\mu_B$/FU. (0.12 $\mu_B$/Fe) at 2 K (Figure 4e). It denotes reminiscence of $Fe^{2+}$-O-$Fe^{2+}$ contacts in the lacunar 2D layers. It should be recalled that in the pristine $Fe^{2+}$ compound, the 2D ferromagnetic ordering occurs below $T_c = 65.5$ K.

In summary, the reversible exsolution of $Fe^{2+}$ ions in a layered Kagomé topology has been shown even at room temperature. It leads to series of novel fully ordered depleted lattices that are able to accommodate a versatile concentration of metal vacancies. To the best of our knowledge, such capacity for "digging and refilling metal holes" with low energy barrier is unique, because even efficient for large dense crystals. This reversible diffusion opens broad possibilities for the prospect of novel materials, but also for the controlled modification of oxides, for example, the transformation of insulators into semiconductors or the achievement of self-regenerative materials. Besides the general interest of low-dimensional electronic materials and their possible connection to magneto-dependent transport, it is worth proposing that the tuning of cation vacancies rather than the standard modification of the anion array could be an alternative to controlling the redox of oxides. Previous evidence for metal exsolution in 3D-olivine compounds and several minerals broadens the panorama of cationic exsolution driven by $Fe^{2+}/Fe^{3+}$ redox. Furthermore, even if Fe centers are involved, similar Fe-exsolutions can be realized from mixed-metallic compounds. For instance, the Fe-depleted mixed $Ba(Fe,Co)_{2-x}(PO_4)_2$ compounds show unexpected magnetic properties and are currently under investigation.

## Experimental Section

Synthesis of the pristine compound $BaFe_2(PO_4)_2$ was described previously.[12] The powder was heated in an alumina crucible, leading to the depleted compound $BaFe_{2-x}(PO_4)_2$. The temperature and the heating times are given in the main text for each sample.

For single-crystal XRD, diffraction data were collected using a DUO-Bruker SMART apex diffractometer (Mo Kα). Intensities were extracted and corrected using the SAINT program.[29] Multi-scan absorption corrections were applied using the SADABS program.[30] The crystal structure refinements were performed using the JANA 2006 program.[31]

Thermogravimetric experiments were carried out on a thermoanalyzer TGA 92 SETARAM under air atmosphere using a ramp of 5 °C min$^{-1}$ to 900 °C after a 1 h step at 100 °C to avoid trace of water.

High-temperature X-ray diffraction was performed in an Anton Paar HTK1200N on a D8 Advance Bruker diffractometer (θ–θ mode, Cu Kα radiation) equipped with a Vantec linear position sensitive detector (PSD). The pattern was recorded in the range 10–80°(2θ) (30 min per scan). Between two patterns the temperature was ramped of 0.08 °C s$^{-1}$ to 900 °C (step $\Delta T = 25$ °C) under 5 L h$^{-1}$ air flow to highlight the iron exsolution and 600 °C under 5 L h$^{-1}$ $H_2/N_2$ (3/97%) gas flow to highlight the iron re-incorporation.

Both magnetization cycles at $T = 2$ and 300 K (up to 5 T) and temperature-dependent magnetic susceptibility of 5.1 mg of $BaFe^{2.5+}_{1.6}(PO_4)_2$ (after washing the free $Fe_2O_3$ particles) were measured using an MPMS squid magnetometer and corrected from diamagnetism. The sample was blocked in a capsule without additional gel to avoid external contributions which can interfere with the hematite signal. The zero field cooling/field cooling (ZFC/FC) procedure was performed at 0.01 T between 2 and 300 K.

Observations by transmission electron Microscopy (TEM) were made on an FEI Technai G220. Observations by scanning electron microscopy (SEM) were made on a Hitachi S400N.

Received: April 22, 2014
Revised: August 7, 2014
Published online: October 24, 2014

**Keywords:** barium · exsolution · iron · reversible topochemical reactions · solid-state reactions

[1] R. Schöllhorn, *Angew. Chem. Int. Ed. Engl.* **1980**, *19*, 983 – 1003; *Angew. Chem.* **1980**, *92*, 477 – 478.
[2] Y. Tsujimoto, C. Tassel, N. Hayashi, T. Watanabe, H. Kageyama, K. Yoshimura, M. Takano, M. Ceretti, C. Ritter, W. Paulus, *Nature* **2007**, *450*, 1062 – 1065.
[3] Y. Kobayashi, O. J. Hernandez, T. Sakaguchi, T. Yajima, T. Roisnel, Y. Tsujimoto, M. Morita, Y. Noda, Y. Mogami, A. Kitada, et al., *Nat. Mater.* **2012**, *11*, 507 – 511.
[4] M. Giorgetti, S. Mukerjee, S. Passerini, J. McBreen, W. H. Smyrl, *J. Electrochem. Soc.* **2001**, *148*, A768 – A774.
[5] R. L. Withers, P. Millet, Y. Tabira, *Z. Für Krist.* **2000**, DOI: 10.1524/zkri.2000.215.6.357.
[6] M. Morcrette, P. Rozier, L. Dupont, E. Mugnier, L. Sannier, J. Galy, J.-M. Tarascon, *Nat. Mater.* **2003**, *2*, 755 – 761.
[7] S. Hamelet, M. Casas-Cabanas, L. Dupont, C. Davoisne, J. M. Tarascon, C. Masquelier, *Chem. Mater.* **2011**, *23*, 32 – 38.
[8] S. Hamelet, P. Gibot, M. Casas-Cabanas, D. Bonnin, C. P. Grey, J. Cabana, J.-B. Leriche, J. Rodriguez-Carvajal, M. Courty, S. Levasseur, et al., *J. Mater. Chem.* **2009**, *19*, 3979 – 3991.
[9] S. Kondoh, M. Kitamura, N. Morimoto, *Am. Mineral.* **1985**, *70*, 737 – 746.
[10] M. Takashi, T. Hiroshi, M. Masamichi, O. Kazumasa, A. Gordon, *Am. Mineral.* **1995**, *80*, 585 – 592.

  

[11] D. Lattard, *Am. Mineral.* **1995**, *80*, 968 – 981.
[12] H. Kabbour, R. David, A. Pautrat, H.-J. Koo, M.-H. Whangbo, G. André, O. Mentré, *Angew. Chem. Int. Ed.* **2012**, *51*, 11745 – 11749; *Angew. Chem.* **2012**, *124*, 11915 – 11919.
[13] R. David, A. Pautrat, D. Filimonov, H. Kabbour, H. Vezin, M.-H. Whangbo, O. Mentré, *J. Am. Chem. Soc.* **2013**, *135*, 13023 – 13029.
[14] D. Dai, M.-H. Whangbo, *Inorg. Chem.* **2005**, *44*, 4407 – 4414.
[15] S. Eymond, M. C. Martin, A. Durif, *Mater. Res. Bull.* **1969**, *4*, 595 – 599.
[16] L. P. Regnault, P. Burlet, J. Rossat-Mignod, *Phys. BC* **1977**, *86 – 88*, *Part 2*, 660 – 662.
[17] M. Heinrich, H.-A. Krug von Nidda, A. Loidl, N. Rogado, R. J. Cava, *Phys. Rev. Lett.* **2003**, *91*, 137601.
[18] N. E. Brese, M. O'Keeffe, *Acta Crystallogr. Sect. B* **1991**, *47*, 192 – 197.
[19] I. A. S. V. I. Pet'kov, *Russ. J. Inorg. Chem.* **2010**, DOI: 10.1134/S0036023610090044.
[20] J. P. Attfield, A. M. T. Bell, L. M. Rodriguez-Martinez, J. M. Greneche, R. Retoux, R. J. Cernik, J. F. Clarke, D. A. Perkins, *J. Mater. Chem.* **1999**, *9*, 205 – 209.
[21] C. M. Srivastava, S. N. Shringi, M. V. Babu, *Phys. Status Solidi A* **1981**, *65*, 731 – 735.
[22] H. Tanaka, *Catal. Surv. Asia* **2005**, *9*, 63 – 74.
[23] R. David, H. Kabbour, S. Colis, A. Pautrat, E. Suard, O. Mentré, *J. Phys. Chem. C* **2013**, *117*, 18190 – 18198.
[24] S. Ishiwata, I. Terasaki, F. Ishii, N. Nagaosa, H. Mukuda, Y. Kitaoka, T. Saito, M. Takano, *Phys. Rev. Lett.* **2007**, *98*, 217201.
[25] X. N. Lin, Z. X. Zhou, V. Durairaj, P. Schlottmann, G. Cao, *Phys. Rev. Lett.* **2005**, *95*, 017203.
[26] W. Bao, Z. Q. Mao, Z. Qu, J. W. Lynn, *Phys. Rev. Lett.* **2008**, *100*, 247203.
[27] "Synthesis of $Fe_2O_3$ nanoparticles by new Sol-Gel method and their structural and magnetic characterizations": A. Shakeel S. K. Hasanain, N. Azmat, M. Nadeem, *arXiv*, **2004**.
[28] J. B. Goodenough, *Magnetism And The Chemical Bond*, Wiley, New York, **1963**.
[29] *SAINT: Area-Detector Integration Software*, Siemens Industrial Automation, Inc.: Madison, WI, **1995**.
[30] *SADABS: Area-Detector Absorption Correction*, Siemens Industrial Automation, Inc.: Madison, WI, **1996**.
[31] V. Petricek, M. Dusek, L. Palatinus, JANA2000 Crystallogr. Comput. Syst. Inst. Phys. Praha Czech Repub. **2000**.